Research Article Vol. 34, No. 7 / 6 Apr 2026 / Optics Express 12493
Optics EXPRESS

Confocal photoluminescence mapping of diamond photonic crystal cavity modes for the silicon vacancy center

LIN JIN,[1,2,3,†,*] MARK ULANOV,[1,†] STEFAN DIETEL,[4] LEV KAZAK,[4] NICOLA LANG,[5] PETER KNITTEL,[5] FEDOR JELEZKO,[4,6] AND WOLFRAM PERNICE[1,2]

[1]*Kirchhoff Institute for Physics, University of Heidelberg, 69120, Germany*
[2]*Institute of Physics and Center for Nanotechnology, University of Münster, 48149, Germany*
[3]*Qutech, Delft University of Technology, 2628 CJ, Netherlands*
[4]*Institute for Quantum Optics, Ulm University, 89081, Germany*
[5]*Fraunhofer Institute for Applied Solid State Physics IAF, 79108, Germany*
[6]*Integrated Quantum Science and Technology (IQST), Ulm University, 89081, Germany*
[†]These authors contributed equally.
[*]*l.jin@tudelft.nl*

Abstract: Diamond photonic crystal cavities offer exceptional properties for interfacing color centers in diamond to integrated photonic circuits. Leveraging Purcell enhancement of the color centers' emission into the zero-phonon line, the development of high quality, low mode volume single-crystal diamond resonators remains one of the key challenges for building diamond quantum networks. In this paper, we present both a robust, versatile photonic crystal design as well as a scalable fabrication process realizing suspended nanobeam cavities. Measurements of confocal microscopy with broadband excitation yield quality factors of more than 5000. We further demonstrate a fast and facile characterization of our structures based on confocal photoluminescence imaging. This method not only provides a more detailed look at the higher order modes within diamond nanobeam resonators but also serves as a non-destructive diagnostic of the modes' susceptibility to fabrication imperfections, providing critical feedback for scalable, high-yield integrated quantum photonic device development.

1. Introduction

Quantum technologies are promising due to their capabilities to tackle problems or stimulate studies that are intractable classically, spanning from the field of computing, communication to sensing [1–3]. A promising route to advance toward quantum technology is leveraging spin qubits based on solid-state defects, thanks to their long coherence time and optical addressability [4,5]. For example, quantum simulators utilizing spin-spin interaction could advance research in areas such as chemical reaction dynamics and many-body physics [6,7]. Furthermore, quantum repeaters enable entanglement swapping over long distances, facilitating secure information transfer across cities [8]. Additionally, sensors based on nitrogen-vacancy (NV) centers in diamond possess exceptional sensitivity in weak magnetic fields, pave the way for applications in medical imaging and mineral exploration [9–11].

Among the platforms that host color centers, diamond outstands for its high Debye temperature and wide bandgap [12,13]. These properties result in a low phonon density, which helps suppress decoherence, and provide a broad optical transparency window, from the ultraviolet to the mid-infrared, allowing efficient interaction with photons across a wide range of wavelengths. As a prominent example NV centers are the most established defect qubits in diamond [14,15]. They demonstrate long coherence times at cryogenic temperatures, and even millisecond at room

#585152 https://doi.org/10.1364/OE.585152
Journal © 2026 Received 18 Nov 2025; revised 26 Jan 2026; accepted 15 Feb 2026; published 27 Mar 2026

Optics EXPRESS

temperature and ambient conditions, which have manifested unprecedented opportunities in applications across quantum networking [16], memory [17], and sensing [18]. However, the fluorescence emission ratio of NVs into zero-phonon line (ZPL) is only around 3% [19], urge its integration to nanophotonic structures. On the other hand, their spin charge states and coherence properties are susceptible to the environmental charge fluctuations [20,21]. This problem can be overcome by group IV color centers in diamond (e.g., silicon vacancy (SiV)) [22]. Due to inversion symmetry [23], SiVs are far less sensitive to electric fields, which ensures stable optical properties like reduced diffusion and transform-limited linewidth [24]. Consequently, integrating SiV centers into nanophotonic structures, such as waveguides and photonic crystal cavities, offers significant opportunities for realizing efficient spin-photon interfaces [25].

The key to diamond spin-photon interfaces lies some of its color centers [15,23]. Once excited, even embedded in waveguides, color centers often decay through phonon-assisted processes, which limits the efficiency of both single-photon generation and photon-mediated entanglement. Therefore, the implementation of photonic crystal cavities becomes essential in pushing the emission occurring in the phonon sideband (PSB) to the ZPL. Efficient spin-photon coupling in diamond color centers hinges on embedding emitters in high-Q, low-mode-volume photonic crystal cavities to leverage strong Purcell enhancement. This boosts emission rates, improves photon collection, and channels emission into well-defined modes, which is key for scalable photonic quantum circuits. For spin-active centers, Purcell enhancement facilitates more robust spin-photon entanglement and readout, enabling efficient integration into complex, on-chip quantum architectures [14,26]. In case of the silicon vacancy (SiV) center, cooperativities above 100 have been reported utilizing photonic crystal cavities [27], which outperforms SiVs embedded in diamond waveguides by several orders of magnitude [28].

Photonic crystal cavities crafted from high-purity, single-crystal diamond are indispensable for quantum computing applications, as even trace impurities can generate unwanted background spin noise and emission that disrupts the detection and manipulation of quantum states associated with diamond color centers. Notably, high-quality single-crystal diamond layers on bulk substrate are still the most easily commercially available substrates, a circumstance that significantly complicates the fabrication of nanophotonic structures when compared to more conventional thin-film platforms [10–12].

Moreover, maximizing Purcell enhancement depends on the precise spectral alignment of a cavity's resonance with the ZPL of the color center [13,14]. Deterministic fabrication of such resonators is limited by fabrication imperfections such as roughness, residual and process-induced impurities and stress. This introduces substantial variations in resonance frequencies. Imaging and understanding these resonators' modes gives insight into the imperfections imposed during the fabrication process, which helps identifying and overcoming these challenges.

In this paper, we propose a photonic crystal cavity design optimized for enhancing the ZPL emission of SiV^- into a cavity mode. The design is adaptable to other color centers in diamond, and resilient to geometric variation over large dimension ranges. Following this fabrication-friendly design, we develop a scalable fabrication process to release nanophotonic cavities on low-cost diamond substrates. Moreover, we perform broadband excitation on the cavities and managed to achieve state-of-the-art quality factors exceeding 5000, which are near the instrumental resolution. Thereafter, we present an imaging study to characterize the mode shape of diamond single-crystal nanobeam cavities. This approach of confocal photoluminescence microscopy is constructive in identifying fabrication imperfections geometry of these nanobeam resonators.

2. Design and numerical optimization of photonic crystal cavities via FDTD

A functional photonic crystal cavity is constructed upon a foundation of a photonic crystal (PhC), a periodic dielectric structure with a refractive index spatially modulated on the wavelength scale [29]. The fundamental building block of the PhC is its unit cell, defined by primitive lattice vector,

Optics EXPRESS

which facilitates the spatial confinement of electromagnetic modes. The periodic boundary conditions give rise to discrete energy levels for each wave vector respectively. These transform into continuous bands within the first Brillouin zone. At the outer edge of the Brillouin zone band gaps form, which prohibit propagation of light frequencies within the PhC. A localized optical mode can be generated at a deterministic position of the PhC by engineering a defect at this position, creating a PhC cavity. PhC nanobeam cavities represent a type of optical resonator that are particularly well-suited for integration with waveguide structures. This integration permits resonant light to be efficiently coupled from the waveguide to the cavity, resulting in substantial enhancement of deterministic photon collection.

Here, we introduce a design framework for high-quality resonators for angled-etching based approaches. As shown in Fig. 1(a) and its inset, the x-axis-oriented diamond waveguide possesses a triangular profile in the yz-plane, characterized by height H and width W. The waveguide's half-apex angle is denoted as θ. A one-dimensional PhC is formed by a periodic array of circular holes with radius R along the x-direction in the center of the waveguide. A PhC cavity is created by introducing a defect region with a parabolically increasing lattice constant. Starting with a minimum lattice constant a_0 at the cavity center, the lattice constant gradually increases until it reaches $a_7 = a$ at the seventh lattice site and then remains constant, extending into the waveguide regions. The lattice constants variation follows $a_N = a \cdot (0.9 + 0.1 \cdot (N/N_0)^2)$ for $N \leq N_0 = 7$. Each side of the cavity contains 20 holes (Fig. 1(b)).

We performed numerical studies on this nanobeam cavity design using the finite-difference time-domain (FDTD) software package MEEP [30]. The cavity with unit lattice period a of 260 nm, a waveguide half-apex angle θ of 45 °, waveguide width W and hole radius R under the manner by introducing weights as W of $1.8a$, and R of $0.285a$ exhibits a fundamental resonant mode at $\lambda_{res,1st} = 740.41$ nm. This mode possesses a high-quality factor (Q-factor) of $Q = 1.82 \times 10^6$ and a small mode volume of $V_m = 0.729 \cdot (\lambda/n)^3$, making the cavity a promising candidate for enhancing SiV- ZPL emission at 737 nm.

Figure 1(c) illustrates the y-component of electric field distribution in the xy-plane (at a z-cut) of the cavity, showing its profile across the entire simulation cell. The field is clearly confined within each cavity segment, reaching maximum intensity at the cavity center. Additionally, the y-component electric field distribution from the side view reveals a higher degree of light penetration into the surrounding air from the top surface of the device compared to the bottom apex (see Supplement 1 Fig. S1 for more details).

We also extracted higher-order resonant modes at longer wavelengths from the simulation. Figure 1(d) depicts the second-order mode ($\lambda_{res,\,2nd} = 764.997\ nm$, $Q = 1.87 \times 10^5$), notable for its asymmetric electric field profile and central node. Figure 1(e) shows the third-order mode ($\lambda_{res,\,3rd} = 782.79\ nm$, $Q = 2067$), which has a symmetric profile with three distinct, bell-shaped maxima. All symmetric modes display an antinode at the cavity center.

Following the initial design, we also conducted a sensitivity analysis on the cavity structure. Extensive parameter sweeps demonstrate a strong correlation between the waveguide half-apex angle and the width. The resonant modes can be preserved by specific geometric adjustments: for every 2.5° increment in half-apex angle θ, widening the waveguide for approximately $0.1a$, while preserving hole radius and cavity period, can keep the resonant performances to that of their initial configuration. Figure 1(f) depicts the correlation between W and θ over a large variation range for achieving resonant modes around a target wavelength of 737 nm. These modes are with consistent high Q-factor and low mode volume, thereby enhancing SiV- ZPL emission. Moreover, this cavity design offers tunability, allowing it to target the emission wavelengths of various other vacancies by adjusting the lattice period (see Supplement 1 S2 and Fig. S2 for more details).

We further investigated the influence of waveguide width W and hole radius R on cavity performance, particularly as these parameters are susceptible to fabrication. The resonance wavelength demonstrated a linear dependency on both W and R, specifically, a 1 nm increase in

Optics EXPRESS

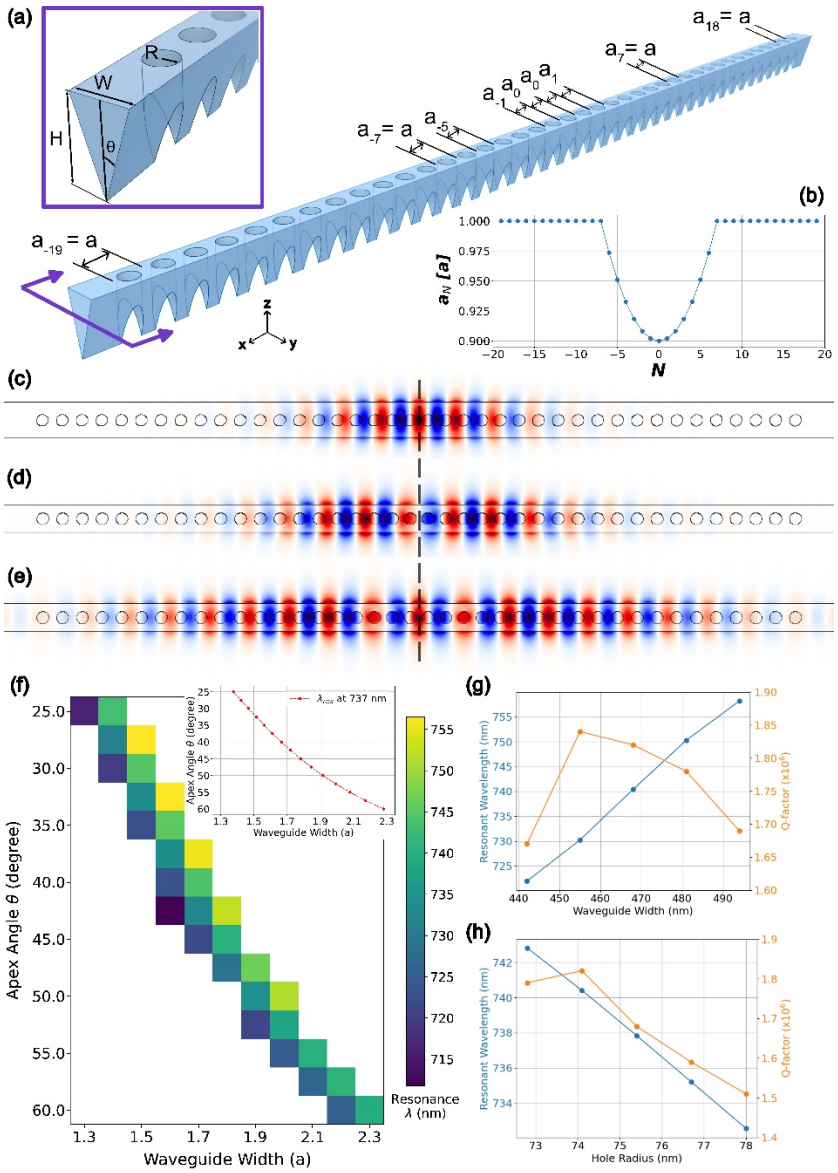

Fig. 1. FDTD simulations of triangular nanobeam cavities. (a) Three-dimensional demonstration of the cavity. (b) Period modulation of the cavity. (c) Fundamental, (d) second-order, and (e) third-order resonant mode (top view) electric field distribution of the y-component at z-cut. (f) Waveguide half-apex angle and width dependency and their impact on the resonant wavelengths of a cavity with lattice period a = 260 nm, hole radius 0.285a. Inset: the correlation between waveguide half-apex angle and width of the cavity to maintain a fundamental resonant mode at 737 nm. (g) The dependency of a cavity's resonance wavelength and Q-factor on waveguide width, when its period a is 260 nm, half-apex angle is 45°, and hole radius is 74.1 nm. (h) The dependency of a cavity's resonance wavelength and Q-factor on hole radius, when its period a is 260 nm, half-apex angle is 45°, and waveguide width is 468 nm.

Optics EXPRESS

W or R yielded a 0.697 nm (Fig. 1(g)) or -1.975 nm (Fig. 1(h)) shift to resonance wavelength, respectively. This linear behavior is consistent with the inherent linearity of Maxwell's equations, which govern the cavity modes as solutions to an eigenvalue problem. From the perspective of quantum perturbation theory [31], small changes in the system, like waveguide width/hole radius variations here, lead to first-order shifts in the eigenvalues (i.e., resonant frequencies) that are proportional to the perturbation. In contrast, the Q-factors remain within the same order of magnitude despite the geometric variations, indicating that deformations are sufficiently small to preserve the cavity's resonant modes. Larger deformations, however, could potentially disrupt the photonic bandgap and compromise cavity functionality.

3. Fabrication

Fabrication of quantum photonic structures requires exceptional material purity, while single-photon-scale quantum computing necessitates an environment with minimal noise [32,33]. Thus, diamond substrates featuring a high-purity single-crystal layer are required for fabricating diamond photonic structures for quantum applications. Single-crystal diamonds are grown by two main techniques: high-pressure-high-temperature (HPHT) or chemical vapor deposition (CVD). Obtaining high-quality single-crystal diamond layers for diamond photonics remains challenging due to the high sensitivity of defect generation to environmental conditions during growth and the quality of the seed substrate [34,35]. HPHT diamonds are typically of high crystal quality, i.e., defect-free, but contain significant amounts of foreign atoms incorporated into the crystal lattice, e.g., nitrogen, boron, nickel, iron, germanium, etc. [36]. Although thin films of single-crystal diamond have recently shown promising results, they generally suffer from thickness variations and imperfect diamond quality [37]. In this work, a thin single-crystal CVD diamond layer grown on thick HPHT diamond substrate was used for fabrication of photonic structures.

To create effective waveguide-based components [38], the structures need to be released from bulk substrate via advanced methods, such as quasi-isotropic etching and angled etching [38–41]. The former requires specific conditions of the process to be fulfilled, such as high plasma densities, elevated temperatures or prolonged etching periods [39,40,42,43], and, thus, require to push the limits of the available equipment. In contrast, Faraday cage angled etching (FCAE) requires just a suitable metal cage and multiple etching steps. In FCAE, the diamond is placed into the metallic cage during the anisotropic plasma etching process. The cages are typically prism or cone shaped. The ions get redirected normal to the sidewall surface, which results in a tilted incidence angle of the ions inside of the cage. This work employs the easily accessible FCAE technique to outline a functional workflow for fabricating high Q-factor ($Q > 10^3$) optical nanocavities designed for 737 nm.

For the fabrication process a 30 µm ultrapure diamond layer was grown on double-side polished (001) HPHT diamond substrates with high crystal quality ($3.1 \times 3.1 \times 0.3$ mm^3, MB Optics, Netherlands). This was achieved using an ellipsoidal microwave plasma chemical vapor deposition (MPCVD) (915 MHz) reactor with purified gases (hydrogen, methane, oxygen) for diamond growth [44]. The growth was performed with all substrates in one run at 8 kW microwave power with a CH_4/H_2 ratio of 1.75%. After growth the samples were polished by scaife polishing to achieve a surface roughness of below 1 nm (RMS). The height of the CVD layer is reduced to 15 µm after polishing.

The samples were then cleaned in a 3:1 mixture of sulfuric and nitric acid at 250 ∘C after polishing. Afterwards the substrate is cleaned in a mixture of equal parts 95-98% sulfuric acid, 65% nitric acid and 70% perchloric acid at 170 ∘C (ETHOS Microwave Digestion System). After that a 200 nm thick layer of silicon nitride (Si_xN_y) is deposited on top of the cleaned surface (PECVD, Oxford Plasmalab) to serve as an etching hard mask.

Optics EXPRESS

To pattern the mask, first a 15 nm-thin aluminum layer is deposited on top of the Si_xN_y layer (Sputtering system, von Ardenne LS 730S). This layer acts as a global charge reservoir, cancelling local charging effects during electron beam patterning. At the next step a 300 nm thick negative resist (Allresist AR-N 7520.18) layer is spin-coated on top of the aluminum mask. The resist is exposed with 100 keV electrons in an electron beam lithography system (Raith EBPG 5150) and consequently developed (Microposit MF-319). Both the unexposed resist and the aluminum are removed by the developer, revealing the Si_xN_y surface. The pattern is transferred to the Si_xN_y hard mask via highly anisotropic reactive ion etching (RIE, Oxford Instruments PlasmaPro 80) in a CHF3/O2 plasma (55 sccm/5 sccm flow rates, 55 mTorr chamber pressure, 175 W RF power). After the ion etching the exposed resist and underlying aluminum are removed by long development in the same developer. The advantage of etching the diamond without the presence of the polymer resist reduces the amount of carbon redeposition leading to smooth diamond surfaces.

The structures are first anisotropically etched using inductively coupled plasma reactive ion etching (ICP, Oxford Instruments PlasmaPro 100 Cobra) in a O2 plasma (50 sccm flow rate, 9/10 mTorr chamber pressure, 800 W ICP power, 200 W RF power, 60◦ C table temperature). The etching is performed in 2 consecutive 2 min steps at 10 and 9 mTorr respectively. This results in a sufficient etching depth of around 800 nm while a plasma-induced mask degradation is reduced to a minimum. Thereafter the diamond substrate is placed in a conical Faraday cage with side angle of 45°. The ions are redirected perpendicular to the surface of the Faraday cage resulting in a circular focal point. Since the focal point of the Faraday cage measures below 1 mm^2, the substrate is precisely repositioned inside the cage for each step in order to cover the entire layout of devices. Due to the focusing of ions, the etching is performed at reduced pressure and RF power (8 mTorr chamber pressure, 200 W ICP power, 10/15 W RF power). Lower RF power leads to a larger half-apex angle. After 2-4 iterations of etching the diamond structures become free-standing with resulting half-apex angles of the structures around 25 ◦.

The tracing of the actual half-apex angle is performed by introducing reference structures consisting of a photonic crystal nanobeam, which is cut-off at the end, revealing its cross-section as shown in Fig. 2(b). This half-hole allows monitoring the hole sidewall verticality in between etching steps. Once the chip layout is sufficiently etched the remaining Si_xN_y hard mask is removed in hydrofluoric acid with subsequent critical point drying in isopropanol. The resulting diamond cavities and reference structures are shown in Fig. 2(a)-(d). More information about the fabrication process can be found in the Supplement 1 S3-S5.

4. Characterization and results

The characterization of the diamond nanocavities is performed at room temperature with a home build confocal microscope. The schematic of the experimental setup is shown in Fig. 3(a). The excitation light is provided by a continuous wave 532 nm laser (Laser Quantum GEM) coupled to the single-mode polarization-maintaining optical fiber (Thorlabs, PM-S405-XP). After the fiber the beam is guided to a beam sampler. The reflected light is focused to a diffraction limited spot onto the diamond sample by an air objective (Olympus, MPlanoApo, 50x, NA 0.95). The laser beam properties after the objective were characterized by the knife edge method (see Supplement 1 S8), resulting in full-width half-maximum of around 510 nm and corresponding Rayleigh length of 1.44 µm. The objective is mounted on a xyz piezo scanner (Npoint, NPXY200-Z25), which allows the objective to travel 200 µm in the x- and y- direction and 25 µm in z-direction. The emitted luminescence light is collected by the same objective and propagates toward the beam sampler. After the beam sampler the light is focused onto 15 µm pinhole, in order to filter out light, which does not originate from the focal volume of the objective. The luminescence light is detected by the avalanche photodiode APD (Excelitas Technology, SPCM-AQRH-15). This

Optics EXPRESS

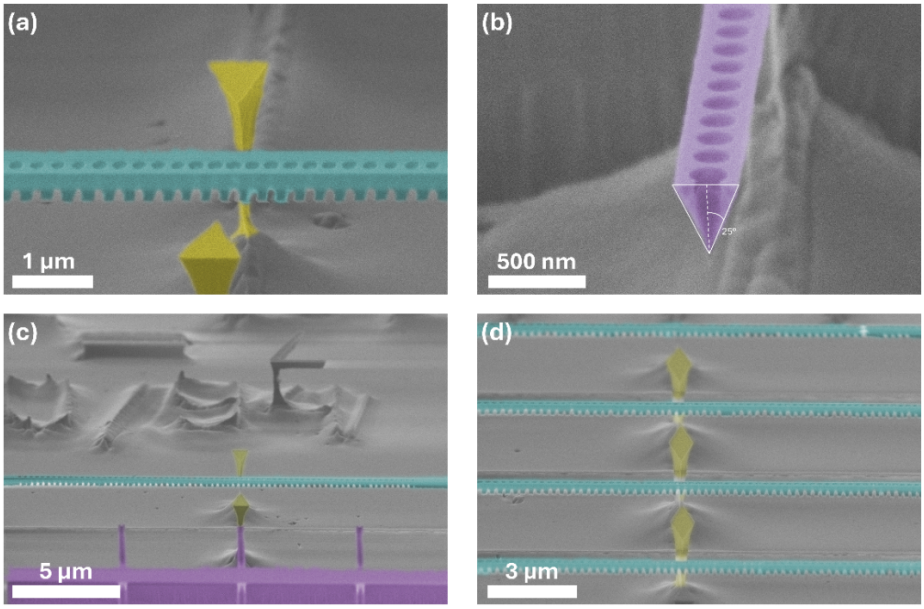

Fig. 2. SEM images of fabricated devices. (a) Photonic crystal cavity (cyan) center indicated by pointer structures (yellow). (b) Reference structure (magenta) allowing for viewing the cross-section of the nanobeams during the multi-step angled etching process. (c) Cavity device with full range of holes on both sides. Additionally, a reference structure with multiple beams (d) matrix of 4 free-standing cavity structures.

allows for recording of confocal maps of the devices from which the nanocavities can be found (see Fig. 3(b)).

Additionally, a motorized flip mirror is positioned after the pinhole, enabling the light to be directed toward the optical spectrometer (Quantum Design, Andor). The spectrometer is equipped by with a Czerny–Turner monochromator (Shamrock-500i) with three diffraction gratings (150 l/mm, blaze 1250 nm; 300 l/mm, blaze 500 nm, 600 l/mm, blaze 500 nm) placed on the motorized turret. The spectrum is recorded by an actively cooled CCD camera (Andor, iDus-DU416A-LDC-DD). The experiment is controlled via a python based modular lab control software package, named Qudi [45]. The integration time for the spectrometer was set as 30 seconds and applied to all measurements in this paper. Figure 3(c) depicts a confocal microscopy spectrum of a cavity acquired using an optical spectrometer with a grating of 600 l/mm. Three prominent peaks were observed. Based on modal spacing between resonant modes, the peak locating at 750.97 nm, 778.03 nm and 796.72 nm were identified as the fundamental, the second order and the third order mode, respectively.

Optical characterization of high-purity diamond photonic crystal cavities necessitates the use of either a tunable laser source covering the relevant spectral range or a broadband excitation approach. The tunable laser enables high-resolution measurement of cavity linewidths and Q-factors of individual resonances, while a broadband excitation allows for simultaneous identification of overall distribution of resonance modes. In this study, we employ off-resonant excitation at 532 nm using a continuous-wave green laser. This wavelength is commonly utilized to excite native color centers, which are randomly generated during growth or aimed species [40,46]. Figure 3(d) demonstrates the photoluminescence spectra acquired by sweeping the focus of the green excitation laser from the device surface ($Z = 0$) into the substrate. A lower Z corresponds to a focus position detuned towards the bottom of the substrate.

Optics EXPRESS

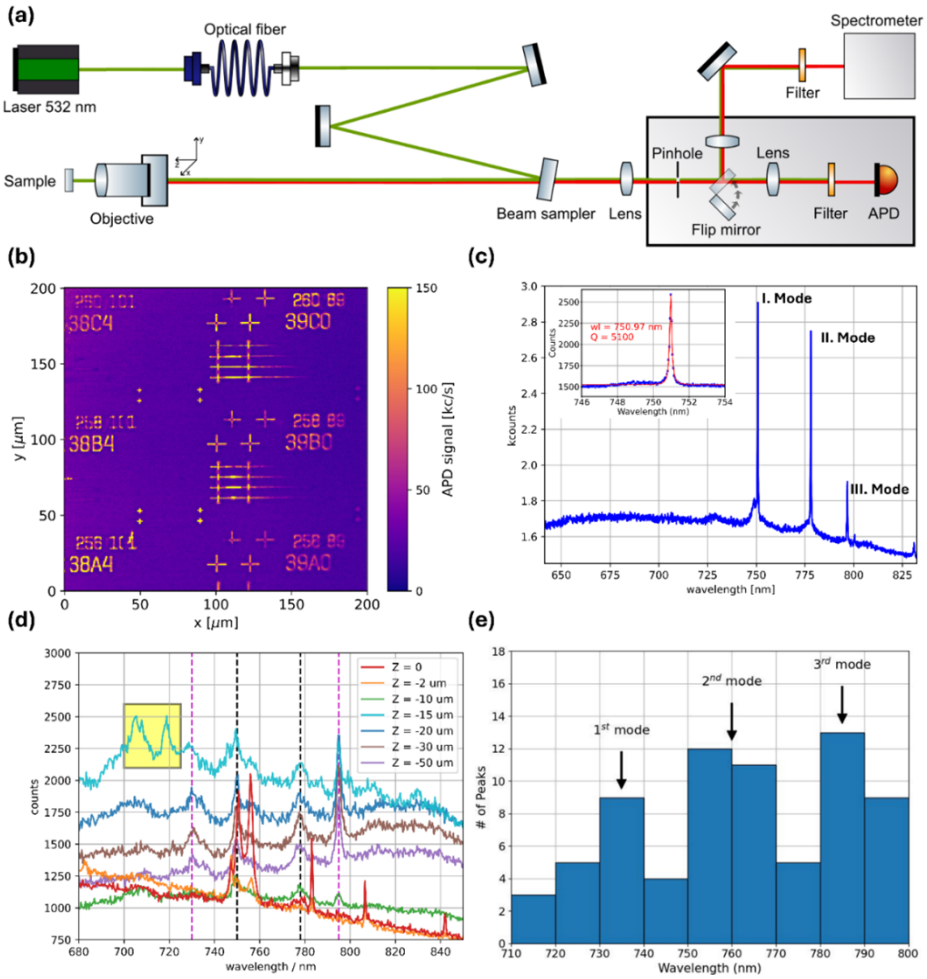

Fig. 3. Confocal photoluminescence measurement. (a) Simplified schematic of the characterization set-up. (b) Photoluminescence map of a section of the fabricated chip. Each device matrix consists of 4 cavities. The cross-like structures above the cavity matrix are reference devices to track the progress of the angular etching in between iterations (c) exemplary spectrum of a cavity center. Inset: Lorentzian fit on the first order mode. (d) Spectra acquired at the *xy*-position of the cavity center for different *z*-positions of the excitation laser's focus. $Z = 0$ corresponds to the device surface. (e) Statistical distribution of high Q-factor resonances. The simulated 3-mode-structure is reflected in the distribution as the peak clusters of the high Q-factor resonances.

The diamond wafer utilized in our experiments consisting of an electronic grade CVD grown on an HPHT substrate [47]. Native color centers were introduced during wafer growth, whose PSB emissions can subsequently serve as broadband light source [37,40,46,48,49]. The maximum broadband emission intensity was confirmed by depth-resolved photoluminescence measurement at $Z = -15$ µm, which corresponds to the interface between the CVD layer and the HPHT substrate. This strong emission signal is attributed to a high concentration of defects at the interface between the two diamond layers.

This broadband signal couples into the photonic crystal cavities, thereby leading to the enhancement of the cavity resonances. We characterized the cavity's spectral performance by

Optics EXPRESS

recording the photoluminescence signal at depth $Z = 0$, observing the fundamental, second, and third order modes at 750.97 nm, 778.03 nm, and 796.72 nm. Furthermore, due to the existence of PBG of the cavity, some signals from the broadband excitation get suppressed, while some get retained. In Fig. 3(d) the spectral peaks pointed out by dashed magenta lines lying above photoluminescence signals, which are pronounced within the bulk diamond, but disappear at its surface, while peaks (at 749 nm and 777 nm) denoted by dashed black lines indicate photoluminescent excitation, which is observed both in the bulk as well as at the surface and device level. Additionally, the retained spectral characteristics from the broadband excitation were consistently observed among all devices on chip. For example, they were also present at the device related to Fig. 3(c) as the left footings of the fundamental and second modes. The depth scan of photoluminescence signal also reveals the location of the main contributors to the spectra. At $Z = -2$ µm, the cavity resonances are still observed but with much less pronounced intensity. Further into the substrate, the spectra become dominated exclusively by features from the native color centers, until the highest intensity of the broadband emission was acquired at $Z = -15$ µm. Moreover, the observation of two distinct peaks (highlighted in yellow) further confirms the high concentrations of color centers existing at the CVD/HPHT interface. Below this depth, the collected signals gradually decreased.

After distinguishing the resonance wavelengths of the cavity modes from other spectral responses, we further extracted their Q-factor values. The finite resolution of the optical spectrometer sets an upper limit of the estimated Q-factor due to sampling. Considering at least 3 points within the FWHM for sufficient fit [50], one can approximate a measurable Q-factor as $Q_{max} \approx \lambda/(3 \cdot \Delta\lambda_S)$, where $\Delta\lambda_S$ is the spectral spacing of the spectrometer. Taking the value of $\Delta\lambda = 0.0456$ nm, the upper limits for the (fundamental, second- and third order) modes are Q_{max} $\approx$ (5500, 5700, 5800). The Q-factors of the resonances are extracted using a Lorentzian fit (see inset Fig. 3(c)).

Following the separation of resonant peaks from the intrinsic diamond substrate signals and the subsequent extraction of the Q-factors, we further statistically analyzed the performance of 170 cavities. Only those with a Q-factor exceeding 1000 were considered, resulting in the spectral distribution histogram depicted in Fig. 3(e). This filtering criterion effectively excludes broad contributions from the diamond substrate, impurities and defects, which typically exhibit low Q values. Master design simulations indicate that for a cavity with a fundamental mode centered around 737 nm, the second and third order modes are positioned approximately 24 nm and another 18 nm away towards longer wavelengths. Figure 3(e) validates this and reveals a clustering of peaks within the wavelength ranges of 730-740 nm, 750-770 nm and 780-790 nm, which corresponds to the respective resonant modes and their characteristic spectral spacings. An additional grouping of peaks is observed in the 790-800 nm range, which is likely attributed to the first few damping modes. Detailed spectral distribution of cavity resonant modes and damping modes are provided in Supplement 1 S6 and S7.

Additionally, we performed a photoluminescence mapping of the resonant modes along one of our devices. The position of the focus is swept in x-direction resulting in a photoluminescence map of the resonant modes' envelope [51]. For one exemplary device (Fig. 3(c)), the nanobeam was probed at different positions along the photonic crystal direction as seen in Fig. 4(a) & (b). The background subtraction is performed with a spectrum taken at a blank position of the nanobeam without any holes. Here three distinct modes at 750.97 nm, 778.03 nm and 796.72 nm are observed and attributed to the first three cavity modes. The most right peak at position 6 and position 7 in Fig. 4(a) appears at around 800 nm and does not correspond to the third-order mode. It is a resonance higher than the third-order mode, which is also vaguely observable at position 5. We attribute this peak to a surface defect such as a localized polish line close to position 6 and 7, when the confocal laser beam shine to its vicinity, it gets excited and feed to the edge of or right after the photonic bandgap, thereafter present as a resonance.

Optics EXPRESS

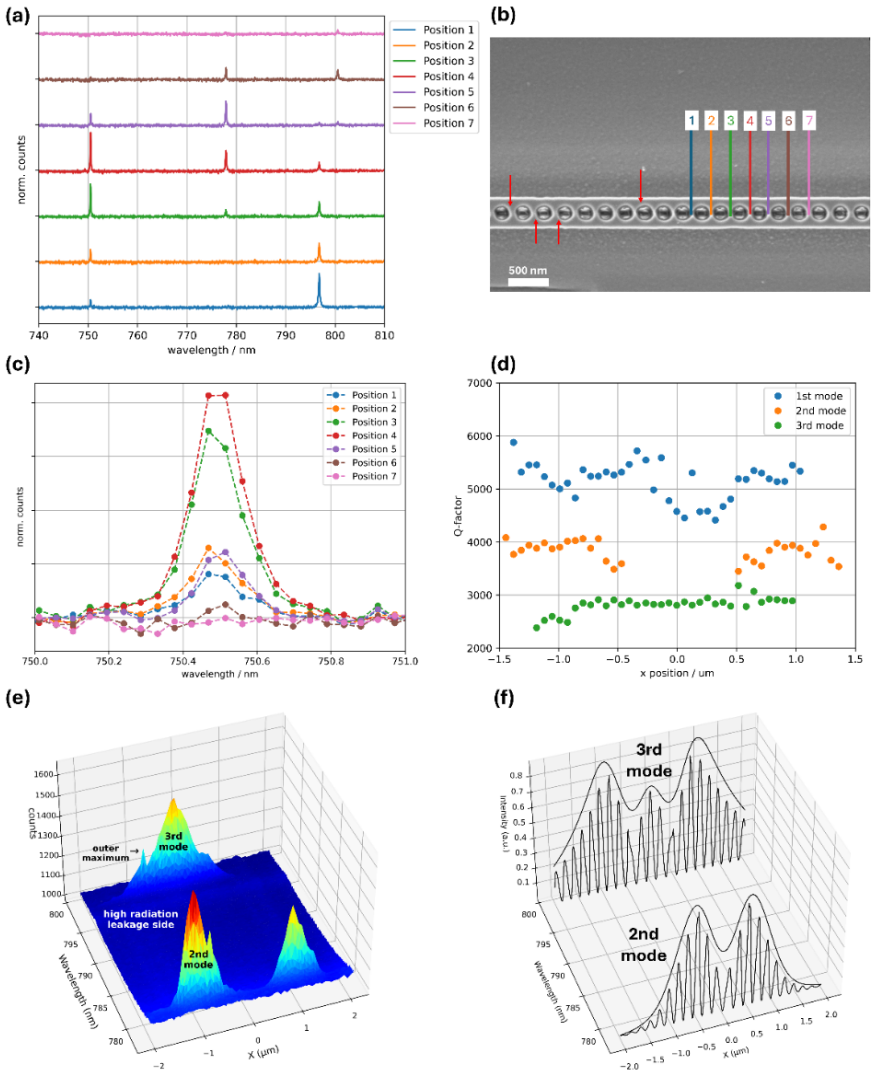

Fig. 4. Confocal mode field measurement. (a) Spectra measured at 7 different points along the nanobeam cavity. (b) Corresponding positions indicated on a top view SEM image of the diamond nanobeam cavity. Position 1 is located exactly at the cavity's center. Red arrows mark imperfections of the hole shape. (c) Zoom-in on the fundamental mode. (d) Q-factor extracted from fitting the resonance along the nanobeam. (e) Photoluminescence spectra of the PhCC near its center along the nanobeam showing the second and third order modes. (f) Time-averaged mode profiles $|E_y(x)|^2$ for the second and third order mode of the cavity obtained from 3D FDTD numerical calculations. The envelope is the result of a convolution with the gaussian beam profile of the confocal volume in x-direction.

The fundamental mode's amplitude is expected to be at its largest in the cavity center due to its spatial mode distribution. Figure 4(c) shows the signals of the fundamental mode when focusing on different positions of the nanobeam. The maximal amplitude and narrowest linewidth are expected in Position 1 & 2. The lack of datapoints for the fundamental mode within its resonance position reflects the effect of the finite resolution of the spectrometer. Thus, the actual maximal amplitude for positions 1 & 2 is not properly recorded. The Q-factors of the first three modes

Optics EXPRESS

were extracted at different focusing positions of the nanobeam, shown in Fig. 4(d). The decrease in Q-factor with higher order modes agrees with the numerical expectation. The fundamental mode's Q-factors being around the resolution limit suggests that the Q-factors of these cavities are even higher, making them comparable to state-of-the-art nanobeam resonators [38,52,53].

The aforementioned works primarily focus on the low-mode-volume fundamental mode and its characterization of Q-factor. While the Q-factor is the most prominent figure-of-merit to quantify the quality of the devices, it reveals little insight in terms of tracing cavity imperfections. To overcome this limitation, here we explicitly investigate the second- and third-order modes of a nanobeam cavity. These modes possess a significantly broader electric field distribution, which is more susceptible to radiation leakage outside of the cavity's center. Hence, this approach can serve as a superior tool for diagnosing and mapping fine fabrication non-idealities across a wide section of devices.

To investigate higher order modes, photoluminescence spectra are taken along the nanobeam. The summarized information obtained from these spectra at different positions can be read as a spatial mapping of the detector signal versus the wavelength and the x-position. The photoluminescence is collected from the APD/spectrometer readout of the confocal volume of the objective (see Fig. 3), which represents the convolution of the focus' gaussian profile in x-direction and the cavity's mode fields [51].

We estimated the finite focus of the confocal microscope as a Gaussian distribution and extracted a qualitative comparison of the mode field measurement to a theoretical calculation [54,55]. The mode electric field distribution at the device surface $|E_y(x)|^2$ is convoluted with a Gaussian beam profile, shown in Fig. 4(f) [51]. It features a widely spread out third order mode, while the photoluminescence measurement in Fig. 4(e) reveals a spatially narrower profile. This discrepancy is attributed to the radiative leakage induced by the surface roughness of the nanobeam cavity. As the period is quadratically tapered, the center of the cavity features a more pronounced surface to volume ratio, therefore the radiative leak is more significant compared to the outer sections. This is evidenced by the stronger confocal photoluminescence intensity from the center field maximum of the third order mode relative to its outer maxima [56,57]. Since the second order mode shows a field minimum in the cavity's center, this effect is not observed here. Furthermore, small distortions in hole roundness on the left-hand side of the resonator (negative x-axis, indicated by red arrows in Fig. 4(b)) are responsible for the increased leak rates in the photoluminescence map. The imperfection manifests in the photoluminescence map as a noticeable intensity asymmetry between the outer maxima of both the second- and third-order in Fig. 4(e). For the third order mode, although the outer maxima generally display lower surface radiation leakage than its central maximum, the localized leakage increase caused by the modestly reduced hole roundness on the left side renders that its photoluminescence maximum is more identifiable than the right side. Numerical studies have addressed the effect of hole roundness deviations on the Q-factor of photonic crystal cavities [58], including their influence on the mode profile would facilitate more quantitative numerical–experimental comparisons. Especially incorporating the unique shape of each distorted hole from scanning electron microscopy analysis into the simulation would shed more light on the distortion of mode profiles based on local distortions beyond the analysis presented in this work.

Furthermore, red shifts of the modes in Fig. 4(a) are 10.08 nm for the fundamental mode, 12.92 nm for the second-order mode and 13.99 nm for the third-order mode with respect to the master design. A global red shift is the result of the dimensions of the fabricated device (366.7 nm width, 101.2 nm hole radius, 30 ∘ half-apex angle) deviating from the designed values. The additional observed relative shift for each mode is attributed to the fabrication distortions resulting in a smaller hole area, thus introducing an extra red shift to each individual resonant mode. Additionally, higher order modes are more affected because of their larger mode field

Optics EXPRESS

distribution along the nanobeam. More data regarding the impact of structure uniformity on the spectrum of a nanobeam resonator can be found in Supplement 1 S6.

5. Conclusion

In this paper, we presented a photonic crystal nanobeam cavity design optimized for enhancing the ZPL emission of SiV^- color centers in diamond. The core strength of this design lies in its adaptability to a range of color centers and its resilience to fabrication-induced geometric variations over large dimensional ranges. Subsequently, we detailed the implementation of a scalable fabrication process that facilitates the monolithic release of these high-performance nanophotonic cavities on cost-effective CVD grown on HPHT diamond substrates, thereby overcoming common constraints associated with bulk diamond.

For the purpose of optical characterization, we strategically leveraged the native color centers present in this layered substrate structure, utilizing their broadband emission spectrum and coupling it to the cavity resonant modes. Through this comprehensive characterization approach, we were able to verify the high quality of the fabricated devices, achieving state-of-the-art Q-factor exceeding 5000. These high Q-factors are limited primarily by the instrumental resolution of our home-built confocal setup, highlighting the success of both the design and fabrication fidelity.

Crucially, we further employed confocal photoluminescence microscopy as an effective mapping study tool to directly characterize the mode shape of the nanobeam cavities. This methodological approach offers a robust and constructive way to identify fabrication imperfections, such as hole shape distortions or surface roughness, and correlate these geometric deviations with measured spectral shifts and spatial characteristics of the resonant modes. More importantly, the methodologies we employed for optical characterization are modular and automatable, facilitating the efficient study of numerous devices with minimal additional overhead. Thus, they provide valuable and rapid feedback to refine and optimize future fabrication processes.

In conclusion, the successful combination of a resilient cavity design, a scalable fabrication method, and an efficient characterization technique establishes a robust photonic platform for engineering solid-state quantum emitters, thereby paving the way for scalable realization of integrated quantum photonic devices and circuitries.

Funding. Bundesministerium für Forschung, Technologie und Raumfahrt (SPINNING 13N16209).

Acknowledgments. The authors thank Cristian Giese for helpful discussions about the fabrication of diamond nanophotonic structures. The authors also thank Ivonne Bente, Dmitrii Raskhodchikov and Simone Ferrari for helpful discussions about electron beam lithography. The authors also thank Katharina Senkhalla and Prithvi Gundlapalli for helpful discussions during the characterization. The fabrication of the devices was carried out at the Münster Nanofabrication Facility, University of Münster, Germany. We thank Michael Ardner (Fraunhofer IAF) for polishing the diamond substrates employed in this work. The characterization of the nanocavities was performed in the laboratories of the Institute for Quantum Optics of the University of Ulm.

Disclosures. The authors declare no conflicts of interest.

Data availability. Data underlying the results presented in this paper are not publicly available at this time but may be obtained from the authors upon reasonable request.

Supplemental document. See Supplement 1 for supporting content.

References

1. J. Chen, "Review on Quantum Communication and Quantum Computation," J. Phys. Conf. Ser. **1865**(2), 022008 (2021).
2. M. Caleffi, M. Amoretti, D. Ferrari, *et al.*, "Distributed quantum computing: A survey," Comput. Netw. **254**, 110672 (2024).
3. Y.-C. Liu, Y.-B. Cheng, X.-B. Pan, *et al.*, "Quantum integrated sensing and communication via entanglement," Phys. Rev. Appl. **22**(3), 034051 (2024).
4. K. C. Miao, J. P. Blanton, C. P. Anderson, *et al.*, "Universal coherence protection in a solid-state spin qubit," Science **369**(6510), 1493–1497 (2020).
5. Z. Zhang, J. Ran, F. Gao, *et al.*, "Operation of Single-Spin Qubits: Recent Advances and Prospects," Adv. Phys. Res. **4**(4), 2400146 (2025).

Optics EXPRESS

6. P. H. Alvarez, F. T. Chowdhury, L. D. Smith, *et al.*, "Simulating spin biology using a digital quantum computer: Prospects on a near-term quantum hardware emulator," APL Quantum **1**(3), 036114 (2024).
7. D. Saha, S. S. Iyengar, P. Richerme, *et al.*, "Mapping Quantum Chemical Dynamics Problems to Spin-Lattice Simulators," J. Chem. Theory Comput. **17**(11), 6713–6732 (2021).
8. A. J. Stolk, K. L. van der Enden, M.-C. Slater, *et al.*, "Metropolitan-scale heralded entanglement of solid-state qubits," Sci. Adv. **10**(44), eadp6442 (2024).
9. L. P. McGuinness, Y. Yan, A. Stacey, *et al.*, "Quantum measurement and orientation tracking of fluorescent nanodiamonds inside living cells," Nat. Nanotechnol. **6**(6), 358–363 (2011).
10. P. Neumann, I. Jakobi, F. Dolde, *et al.*, "High-Precision Nanoscale Temperature Sensing Using Single Defects in Diamond," Nano Lett. **13**(6), 2738–2742 (2013).
11. I. Lovchinsky, A. O. Sushkov, E. Urbach, *et al.*, "Nuclear magnetic resonance detection and spectroscopy of single proteins using quantum logic," Science **351**(6275), 836–841 (2016).
12. C. E. Nebel, "Nitrogen-vacancy doped CVD diamond for quantum applications: A review," *Semiconductors and Semimetals, Diamond for Quantum Applications* Part 1, 103, Chap. 4, pp. 73–136 (Elsevier, 2020)
13. M. O. de Vries, B. del Rosal, K. A. Messalea, *et al.*, "All-Optical Thermometry with Infrared Emitting Defects in Diamond," Adv. Sens. Res. **3**(1), 2300086 (2024).
14. R. Katsumi, K. Takada, F. Jelezko, *et al.*, "Recent progress in hybrid diamond photonics for quantum information processing and sensing," Commun. Eng. **4**(1), 85 (2025).
15. L. V. H. Rodgers, L. B. Hughes, M. Xie, *et al.*, "Materials challenges for quantum technologies based on color centers in diamond," MRS Bull. **46**(7), 623–633 (2021).
16. C. E. Bradley, S. W. de Bone, P. F. W. Möller, *et al.*, "Robust quantum-network memory based on spin qubits in isotopically engineered diamond," Npj Quantum Inf. **8**(1), 122 (2022).
17. C. E. Bradley, J. Randall, M. H. Abobeih, *et al.*, "A Ten-Qubit Solid-State Spin Register with Quantum Memory up to One Minute," Phys. Rev. X **9**(3), 031045 (2019).
18. B. Bürgler, T. F. Sjolander, O. Brinza, *et al.*, "All-optical nuclear quantum sensing using nitrogen-vacancy centers in diamond," Npj Quantum Inf. **9**(1), 56 (2023).
19. M. Gould, E. R. Schmidgall, S. Dadgostar, *et al.*, "Efficient Extraction of Zero-Phonon-Line Photons from Single Nitrogen-Vacancy Centers in an Integrated GaP-on-Diamond Platform," Phys. Rev. Appl. **6**(1), 011001 (2016).
20. Z. Yuan, M. Fitzpatrick, L. V. H. Rodgers, *et al.*, "Charge state dynamics and optically detected electron spin resonance contrast of shallow nitrogen-vacancy centers in diamond," Phys. Rev. Res. **2**(3), 033263 (2020).
21. R. Giri, R. H. Jensen, D. Khurana, *et al.*, "Charge Stability and Charge-State-Based Spin Readout of Shallow Nitrogen-Vacancy Centers in Diamond," ACS Appl. Electron. Mater. **5**(12), 6603–6610 (2023).
22. B. Pingault, D.-D. Jarausch, C. Hepp, *et al.*, "Coherent control of the silicon-vacancy spin in diamond," Nat. Commun. **8**(1), 15579 (2017).
23. C. Hepp, T. Müller, V. Waselowski, *et al.*, "Electronic Structure of the Silicon Vacancy Color Center in Diamond," Phys. Rev. Lett. **112**(3), 036405 (2014).
24. D. D. Sukachev, A. Sipahigil, C. T. Nguyen, *et al.*, "Silicon-Vacancy Spin Qubit in Diamond: A Quantum Memory Exceeding 10 ms with Single-Shot State Readout," Phys. Rev. Lett. **119**(22), 223602 (2017).
25. C. M. Knaut, A. Suleymanzade, Y.-C. Wei, *et al.*, "Entanglement of nanophotonic quantum memory nodes in a telecom network," Nature **629**(8012), 573–578 (2024).
26. R. A. Parker, J. Arjona Martínez, K. C. Chen, *et al.*, "A diamond nanophotonic interface with an optically accessible deterministic electronuclear spin register," Nat. Photonics **18**(2), 156–161 (2024).
27. M. K. Bhaskar, R. Riedinger, B. Machielse, *et al.*, "Experimental demonstration of memory-enhanced quantum communication," Nature **580**(7801), 60–64 (2020).
28. M. K. Koch, M. Hoese, V. Bharadwaj, *et al.*, "Super-Poissonian Light Statistics from Individual Silicon Vacancy Centers Coupled to a Laser-Written Diamond Waveguide," ACS Photonics **9**(10), 3366–3373 (2022).
29. J. D. Joannopoulos, S. G. Johnson, J. N. Winn, *et al.*, *Photonic Crystals: Molding The Flow Of Light*, 2nd ed. (Princeton University Press, 2008).
30. A. F. Oskooi, D. Roundy, M. Ibanescu, *et al.*, "Meep: A flexible free-software package for electromagnetic simulations by the FDTD method," Comput. Phys. Commun. **181**(3), 687–702 (2010).
31. T. Kato, *Perturbation Theory for Linear Operators*, 2nd ed. (Springer, 1995).
32. S. Bogdanov, M. Y. Shalaginov, A. Boltasseva, *et al.*, "Material platforms for integrated quantum photonics," Opt. Mater. Express **7**(1), 111–132 (2017).
33. L. Ma, O. Slattery, and X. Tang, "Noise reduction in optically controlled quantum memory," Mod Phys Lett B **32**(14), 1830001 (2018).
34. P. M. Martineau, M. P. Gaukroger, K. B. Guy, *et al.*, "High crystalline quality single crystal chemical vapour deposition diamond," J. Phys. Condens. Matter **21**(36), 364205 (2009).
35. Y. Ren, W. Lv, X. Li, *et al.*, "Effect of nitrogen on growth and optical properties of single-crystal Diamond synthesized by chemical vapor deposition," Mater. Basel **17**(6), 1311 (2024).
36. U. F. S. D'Haenens-Johansson, J. E. Butler, and A. N. Katrusha, "Synthesis of Diamonds and Their Identification," Rev. Mineral. Geochem. **88**(1), 689–753 (2022).
37. S. W. Ding, M. Haas, X. Guo, *et al.*, "High-Q cavity interface for color centers in thin film diamond," Nat. Commun. **15**(1), 6358 (2024).

Optics EXPRESS

38. M. J. Burek, Y. Chu, M. S. Z. Liddy, *et al.*, "High quality-factor optical nanocavities in bulk single-crystal diamond," Nat. Commun. **5**(1), 5718 (2014).
39. B. Khanaliloo, M. Mitchell, A. C. Hryciw, *et al.*, "High-Q/V Monolithic Diamond Microdisks Fabricated with Quasi-isotropic Etching," Nano Lett. **15**(8), 5131–5136 (2015).
40. S. Mouradian, N. H. Wan, T. Schröder, *et al.*, "Rectangular photonic crystal nanobeam cavities in bulk diamond," Appl. Phys. Lett. **111**(2), 021103 (2017).
41. P. Latawiec, M. J. Burek, Y.-I. Sohn, *et al.*, "Faraday cage angled-etching of nanostructures in bulk dielectrics," J. Vac. Sci. Technol. B **34**(4), 041801 (2016).
42. C. Dory, D. Vercruysse, K. Y. Yang, *et al.*, "Inverse-designed diamond photonics," Nat. Commun. **10**(1), 3309 (2019).
43. M. Pasini, N. Codreanu, T. Turan, *et al.*, "Nonlinear Quantum Photonics with a Tin-Vacancy Center Coupled to a One-Dimensional Diamond Waveguide," Phys Rev Lett. **133**(2), 023603 (2024).
44. M. Füner, C. Wild, and P. Koidl, "Novel microwave plasma reactor for diamond synthesis," Appl. Phys. Lett. **72**(10), 1149–1151 (1998).
45. J. M. Binder, A. Stark, N. Tomek, *et al.*, "Qudi: A modular python suite for experiment control and data processing," SoftwareX **6**, 85–90 (2017).
46. L. Li, T. Schröder, E. H. Chen, *et al.*, "Coherent spin control of a nanocavity-enhanced qubit in diamond," Nat. Commun. **6**(1), 6173 (2015).
47. A. M. Zaitsev, *Optical Properties of Diamond*, 1st ed. (Springer, 2001).
48. A. E. Rugar, S. Aghaeimeibodi, D. Riedel, *et al.*, "Quantum Photonic Interface for Tin-Vacancy Centers in Diamond," Phys. Rev. X **11**(3), 031021 (2021).
49. N. H. Wan, S. Mouradian, and D. Englund, "Two-dimensional photonic crystal slab nanocavities on bulk single-crystal diamond," Appl. Phys. Lett. **112**(14), 141102 (2018).
50. J. G. Robertson, "Detector Sampling of Optical/IR Spectra: How Many Pixels per FWHM?" Publ. Astron. Soc. Aust. **34**, e035 (2017).
51. F. S. F. Brossard, B. P. L. Reid, C. C. S. Chan, *et al.*, "Confocal microphotoluminescence mapping of coupled and detuned states in photonic molecules," Opt. Express **21**(14), 16934–16945 (2013).
52. A. Sipahigil, R. E. Evans, D. D. Sukachev, *et al.*, "An integrated diamond nanophotonics platform for quantum-optical networks," Science **354**(6314), 847–850 (2016).
53. M. J. Burek, C. Meuwly, R. E. Evans, *et al.*, "Fiber-Coupled Diamond Quantum Nanophotonic Interface," Phys Rev Appl. **8**(2), 024026 (2017).
54. S. Stallinga and B. Rieger, "Accuracy of the Gaussian Point Spread Function model in 2D localization microscopy," Opt. Express **18**(24), 24461–24476 (2010).
55. M. J. Nasse and J. C. Woehl, "Realistic modeling of the illumination point spread function in confocal scanning optical microscopy," J. Opt. Soc. Am. A **27**(2), 295–302 (2010).
56. B. E. Little and S. T. Chu, "Estimating surface-roughness loss and output coupling in microdisk resonators," Opt. Lett. **21**(17), 1390–1392 (1996).
57. M. Borselli, T. J. Johnson, and O. Painter, "Accurate measurement of scattering and absorption loss in microphotonic devices," Opt. Lett. **32**(20), 2954–2956 (2007).
58. Y. Yamaguchi, S. W. Jeon, B. S. Song, *et al.*, "Analysis of Q-factors of structural imperfections in triangular cross-section nanobeam photonic crystal cavities," J. Opt. Soc. Am. B **32**(9), 1792–1796 (2015).